



## Effect of strontium on the structural and piezoelectric properties of the sol gel processed barium titanate

A. El ghandouri<sup>1</sup>, S. Sayouri<sup>1</sup>, T. Lamcharfi<sup>2</sup>, L. Hajji<sup>3</sup>

<sup>1</sup>Laboratory of Physics, Theoretical and Applied, FSDM B.P. 179, Fez, Morocco

<sup>2</sup>Laboratory of signals systems and components, FST Street Immouzar, B.P. 2202 Fez, Morocco

<sup>3</sup>LMCN, F.S.T.G University Cadi Ayyad Marrakech, Morocco

Received 25 Jul 2017,

Revised 17 Oct 2017,

Accepted 24 Oct 2017

### Keywords

- ✓ (Ba, Sr)TiO<sub>3</sub> ceramics,
- ✓ Sol Gel,
- ✓ Dielectric properties,
- ✓ Complex impedance,
- ✓ PTCR,
- ✓ Piezoelectric properties.

[S.Sayouri@gmail.com](mailto:S.Sayouri@gmail.com) ;

Phone: +212673785288;

### Abstract

Structural, dielectric and piezoelectric properties of nanopowders of pure and strontium-doped BaTiO<sub>3</sub> (Ba<sub>1-x</sub>Sr<sub>x</sub>)TiO<sub>3</sub> (x = 0.00; 0.10; 0.20; 0.30 and 0.40), synthesized by the sol gel process, have been investigated. The samples crystallize in the pure perovskite structure and transform from tetragonal to pseudocubic under doping with Sr. The calculated average crystallite size was about 30 nm. Dielectric parameters (dielectric permittivity and losses) were determined. Sr doping gives rise to a decrease of the ferro-to-paraelectric transition temperature and to an enhancement of the Positive Temperature Coefficient of Resistivity (PTCR). Piezoelectric parameters were also determined and their thermal behavior investigated.

## 1. Introduction

Barium Titanate (BaTiO<sub>3</sub>) is a perovskite type material, which is known for its various properties: high dielectric constant, ferroelectric behavior below 130 °C, spontaneous polarization and non-linear optical coefficients. The origin of ferroelectricity in BaTiO<sub>3</sub> derives from the displacement of ions relative to each other. It is well known that dielectric properties of BaTiO<sub>3</sub> can be systematically modified by chemical substitution of barium and/or titanium by a wide variety of isovalent and aliovalent dopants. The study of this lead-free compound is interesting not only for basic research but also for its applications in many industrial sectors, such as Multilayer Ceramic (MLCCs), non-volatile ferroelectric FRAM's memories, detection of gaseous pollutants like CO, Positive temperature coefficient resistors (PTCR), optical data storage at High density, ultrasonic transducer [1-5].

Strontium-doped barium titanate (BST) has been widely used for various applications, particularly in the fields of electronics and telecommunications, because of its high dielectric constant, large electric field tunabilities, relatively low dielectric losses, variable Curie temperature depending on Sr content, large polarization and large induced strains [6-9].

The aim of the present work is the synthesis, by the sol gel process, and characterization of pure and strontium doped BaTiO<sub>3</sub> materials, in view of investigation of the influence of Sr-doping on their structural microstructural and dielectric properties. It is known that synthesis of BaTiO<sub>3</sub> by conventional methods needs high calcination temperatures [10]. In this regard, Our interest consists also in optimizing this parameter. To this end, we have prepared a series of sol gel processed Sr-doped BT, which chemical formula is Ba<sub>1-x</sub>Sr<sub>x</sub>Ti<sub>1+x/4</sub>O<sub>3</sub>, through the destabilization of colloidal solution (DCS) method, and their structure and dielectric properties were investigated.

## 2. Experimental procedure

### 2.1. Samples preparation

Strontium-doped barium titanate powders, (Ba<sub>1-x</sub>Sr<sub>x</sub>)TiO<sub>3</sub> (BST<sub>x</sub>), were prepared by the sol-gel route using titanium isopropoxide: Ti[OCH(CH<sub>3</sub>)<sub>2</sub>]<sub>4</sub> (purity ≥97%), Barium acetate C<sub>4</sub>H<sub>6</sub>Ba O<sub>4</sub> (99%), strontium acetate C<sub>4</sub>H<sub>6</sub>SrO<sub>4</sub> as precursors, in adequate proportions.

Distilled water, acetic acid  $\text{CH}_3\text{COOH}$  and ethanol  $\text{C}_2\text{H}_5\text{OH}$  as solvent.

The following flow chart details the experimental procedure of preparation of the samples.

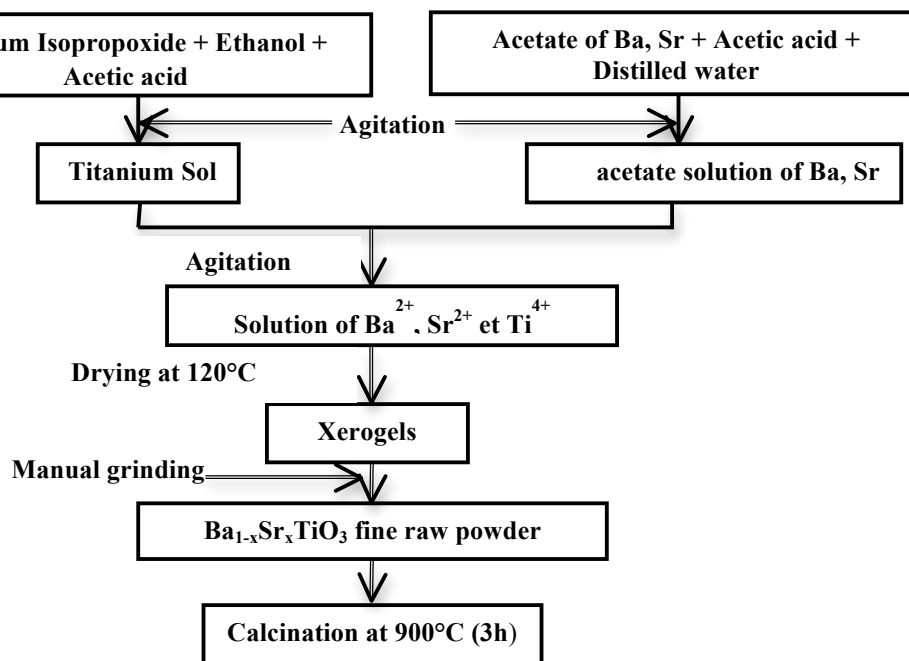


Figure 1: Flow chart of the preparation of  $\text{BST}_x$  samples

## 2.2. Characterisation equipment

Crystal structures of  $\text{Ba}_{1-x}\text{Sr}_x\text{TiO}_3$  powders were determined by X-ray diffraction (XRD) using a  $\text{CuK}\alpha$  radiation ( $\lambda = 1.54059 \text{ \AA}$ ), FTIR spectra and Raman spectra. Microstructure of powders and ceramics was characterized using a scanning electron microscope (SEM) (Quanta 200 FEI). For dielectric measurements, the powders were compressed into discs of about 12mm as diameter and sintered at  $1200^\circ\text{C}$  for 6 hrs.

The dielectric properties were measured by an impedance analyzer (HP 4284A), in the temperature and frequency ranges [ambiente,  $500^\circ\text{C}$ ] and [20 Hz, 1MHz], respectively.

## 3. Results and discussion

### 3.1. Structural characterizations

Figure 2(a) shows XRD patterns of the BT powders calcined at  $800^\circ\text{C}$  and  $900^\circ\text{C}$ , revealing that the formation of the pure  $\text{BaTiO}_3$  phase is complete at  $900^\circ\text{C}$ . Zoom in on the peak (110) shows a shifting of this peak to lower angles, and hence an improvement in powder crystallinity by increasing the calcination temperature from  $800^\circ\text{C}$  to  $900^\circ\text{C}$  (Fig. 2(b)).

Table 1 shows FWHM to decrease with increasing temperature indicating an increase in the crystallite size.

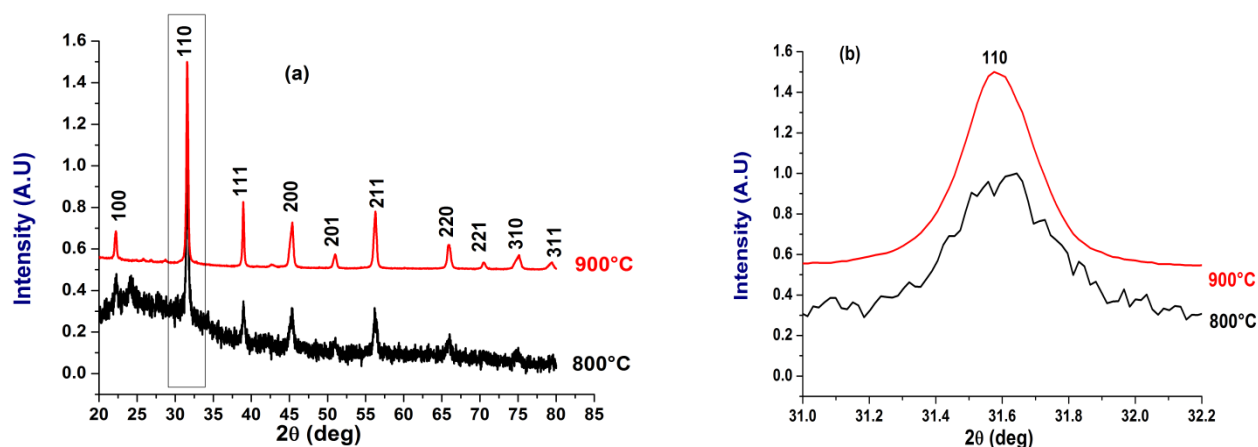


Figure 2: (a) XRD pattern of BT powders calcined at 800 and  $900^\circ\text{C}$ , (b) zoom in on the peak (110).

**Table 1:** Structural parameters of BT powders calcined at different temperatures

Calcination temperature	2 $\theta$	hkl	FWHM	Crystallite size (nm)	d-spacing( $^{\circ}$ A)
800 $^{\circ}$ C	31.6055	110	0.2342	35.25	2.8309
900 $^{\circ}$ C	31.5541	110	0.2175	37.95	2.8331

Figure 3 shows XRD diffractograms of Ba<sub>1-x</sub>Sr<sub>x</sub>TiO<sub>3</sub> (x = 0.00; 0.10; 0.20; 0.30 and 0.40) powders calcined at 900 $^{\circ}$ C during 3h, showing that all samples crystallize in the pure perovskite phase, but however with the presence of few traces of impurities. This result is consistent with several other studies [11- 13].

Furthermore, since the strontium doping rate was increased, the diffraction peaks slightly shift toward higher angles, as shown in figure 3(b); indeed, zoom in on the peak (111) in the range 38  $^{\circ}$  <2 $\theta$  <40  $^{\circ}$  shows clearly that Sr-doping moves the position of this peak towards highest angles. The BaTiO<sub>3</sub> lattice is contracted by incorporation of Sr atoms as the ionic radii of Ba<sup>2+</sup> and Sr<sup>2+</sup> are 1.49 and 1.32  $\text{Å}$ , respectively, and then a lattice distortion would be induced. Sr-doping gives rise to a slight transformation from quadratic (pure BT) to pseudocubic phase (BST<sub>x</sub>, x > 0.20) as revealed by the zoom in on the peak (200) in the range 44  $^{\circ}$  <2 $\theta$  <47  $^{\circ}$ , showing that this large and asymmetric peak indicates *the existence of two complementary peaks* is clearly, *observed around 2 $\theta$  = 45 $^{\circ}$ 09' and 2 $\theta$  = 45 $^{\circ}$ 36'* in the pure sample (x = 0), and these two peaks tend to merge as observed for the three other compositions (Fig. 3c) while maintaining relatively large FWHM. Stabilization of the pseudocubic has also been reported [14].

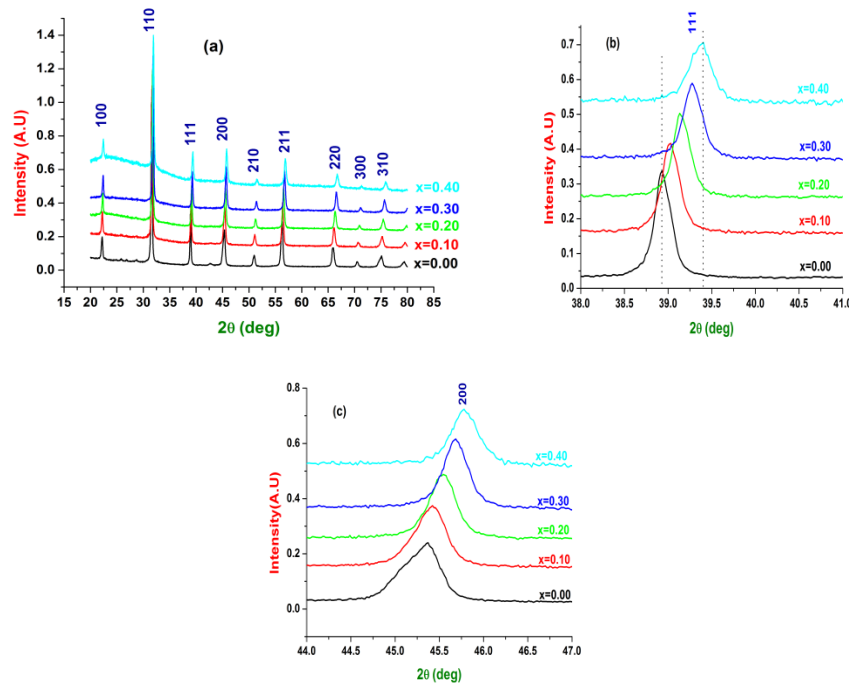


**Figure 3:** (a) XRD pattern of Ba<sub>1-x</sub>Sr<sub>x</sub>TiO<sub>3</sub> powders calcined at 900  $^{\circ}$ C for 3h, (b) zoom in on (111) peak and (c) zoom in on (200) peak.

The average crystallite size (ACS) of the Ba<sub>1-x</sub>Sr<sub>x</sub>TiO<sub>3</sub> samples was calculated using the Scherrer formula:

$$T_G = \frac{K * \lambda}{FWHM * \cos \theta} \quad (1)$$

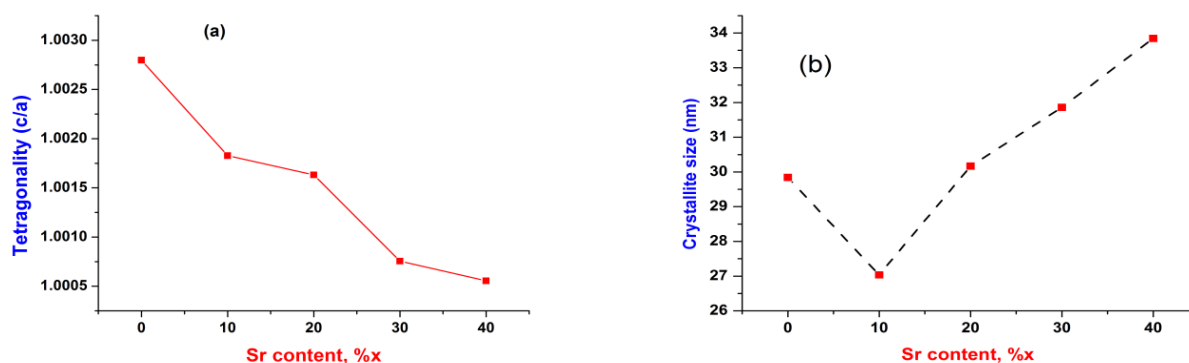
Where K = 0.9 is a constant,  $\lambda$  = 0.154059 nm is the wavelength of the source used and FWHM is the half-height width [15].

Table 2 shows the estimated average crystallite size of the as-prepared Ba<sub>1-x</sub>Sr<sub>x</sub>TiO<sub>3</sub> powders calcined at 900 $^{\circ}$ C for 3 h, assuming spherical shaped particles. It is observed that the ACS first decreases (x = 0.10) and then increases (x = 0.20, 0.30 and 0.40).

Figure 4 and Table 2 show that as the strontium content increases, the tetragonality of the structure decreases, and that for x>0.20 in Sr, the structure stabilizes in the pseudo cubic one, due to electrostatic repulsions between 3d electrons of Ti<sup>4+</sup> ions and 2p electrons of O<sup>2-</sup> ions [16]. On the other hand, the elementary cell volume is reduced with Sr doping as seen in Table 2, probably due to the smaller ionic radius of Sr<sup>2+</sup> (1.32  $^{\circ}$ A) compared to that of Ba<sup>2+</sup> (1.49  $^{\circ}$ A).

**Table 2:** Variation of lattice parameters, tetragolality, volume and crystallite size of  $\text{Ba}_{1-x}\text{Sr}_x\text{TiO}_3$  powders calcined at 900 °C for 3 h.

$(\text{Ba}_{1-x}\text{Sr}_x)\text{TiO}_3$	Lattice parameters			tetragolality	Structure	Volume ( $\text{\AA}^3$ )	Average crystallite size (nm)
	X	a (°A)	b (°A)				
0.00	4.0023	4.0023	4.0135	1.0028	Tetragonal	64.29	29.8401
0.10	3.9952	3.9952	4.0025	1.0018	Tetragonal	63.89	27.0336
0.20	3.9831	3.9831	3.9896	1.0016	Tetragonal	63.30	30.1661
0.30	3.9715	3.9715	3.9745	1.0007	Pseudo Cubic	62.69	31.8600
0.40	3.9638	3.9638	3.9660	1.0005	Pseudo Cubic	62.31	33.8436



**Figure 4:** (a) Variation of tetragolality and lattice parameters of  $\text{Ba}_{1-x}\text{Sr}_x\text{TiO}_3$  powders calcined at 900 °C for 3 h, (b) average crystallite size vs. x

Figure 5 (a) shows the FTIR spectra of the  $\text{Ba}_{1-x}\text{Sr}_x\text{TiO}_3$  powders for different concentrations in Sr. The absorption band in the low frequency range from  $400\text{ cm}^{-1}$  to  $800\text{ cm}^{-1}$ , derived from the vibrations (vibrations of the  $\text{TiO}_6$  octahedron) of the Ti-O isopropoxide groups [17]. Two intense bands at  $1430$  and  $1556\text{ cm}^{-1}$  are assigned to symmetrical and antisymmetric vibrations respectively (stretching of barium and / or titanium-bound carboxylic groups ( $\text{COO}^-$ )) [18, 19]. Two bands lying between  $1000$  and  $1200\text{ cm}^{-1}$  can be attributed to isopropyl groups bound to the titanium atoms in a monodentate mode and traces of the carbonate in small amount. The vibration band of the organic (carboxylic) groups, located in the frequency range between  $900$  and  $1700\text{ cm}^{-1}$ , decreased with the increase of the strontium doping rate (it disappeared for  $x = 0.40$ , in conformity with XRD results), while the Ti-O absorption peaks become more prominent.

Figure 5 (b) shows the Raman spectra of the  $\text{Ba}_{1-x}\text{Sr}_x\text{TiO}_3$  nano-powders obtained for different Sr content. The active Raman modes for  $\text{BaTiO}_3$  characterizing the quadratic phase are displayed. The sharp bands around  $189\text{ cm}^{-1}$   $A_1(\text{LO})$  and  $307\text{ cm}^{-1}$   $[B_1, E(\text{TO} + \text{LO})]$  and the wide bands around  $262\text{ cm}^{-1}$   $[A_1(\text{TO}), E(\text{TO})]$  and  $716\text{ cm}^{-1}$   $[A_1(\text{LO}), E(\text{LO})]$  are characteristic peaks of the quadratic phase of  $\text{BaTiO}_3$  [20, 21].

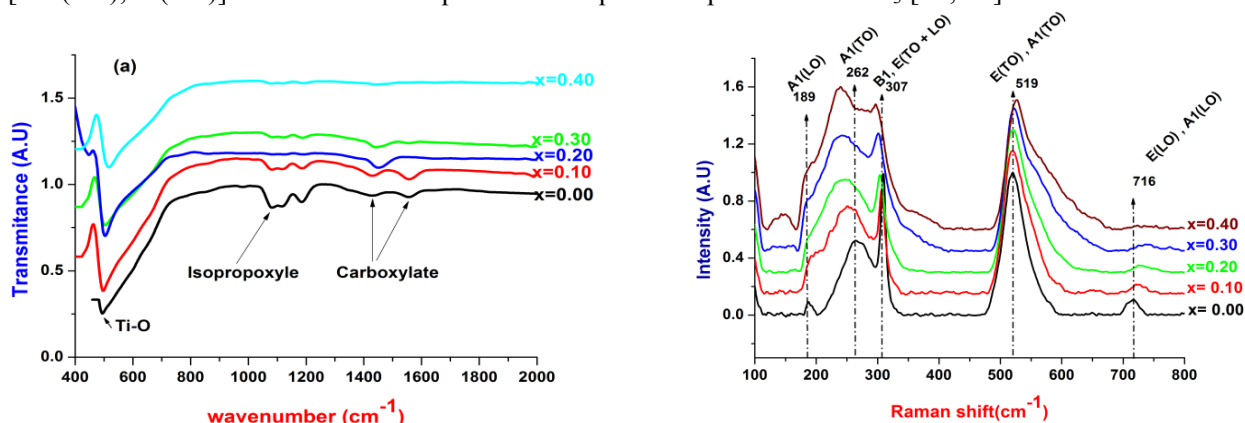


**Figure 5:** (a) FTIR Spectra, (b) Raman spectra of  $\text{Ba}_{1-x}\text{Sr}_x\text{TiO}_3$  calcined at 900°C for 3h

It is observed on these Raman spectra that as x increases ( $x > 0$ ), intensities of the peaks mentioned above decrease with a slight frequency range shift, pointing out the effect of Sr on the BT structure. In particular, the peak intensity of the band located at  $716\text{ cm}^{-1}$  characteristic of the quadratic phase, undergoes a strong decrease

( $x > 0.20$ ), indicating the transition from quadratic to pseudo cubic phase. Observations made on Raman spectra are in good agreement of those of revealed by XRD analysis.

### 3.2. SEM characterization

Figures 6 (a) and (b) show the SEM micrographs of  $\text{Ba}_{1-x}\text{Sr}_x\text{TiO}_3$  ( $x = 0.20$  and  $0.30$ ) samples sintered at  $1200^\circ\text{C}$  for 6h. These images show well-developed grain morphology and a dense microstructure. The mean grain size, estimated for the whole range of  $x$ , varies between  $3.6\ \mu\text{m}$  ( $x = 0.00$ ) to  $830\ \text{nm}$  ( $x = 0.40$ ). This result may be associated with the substitution of the larger  $\text{Ba}^{2+}$  ion by the smaller  $\text{Sr}^{2+}$  ion, structural defects, or the formation of agglomerates.

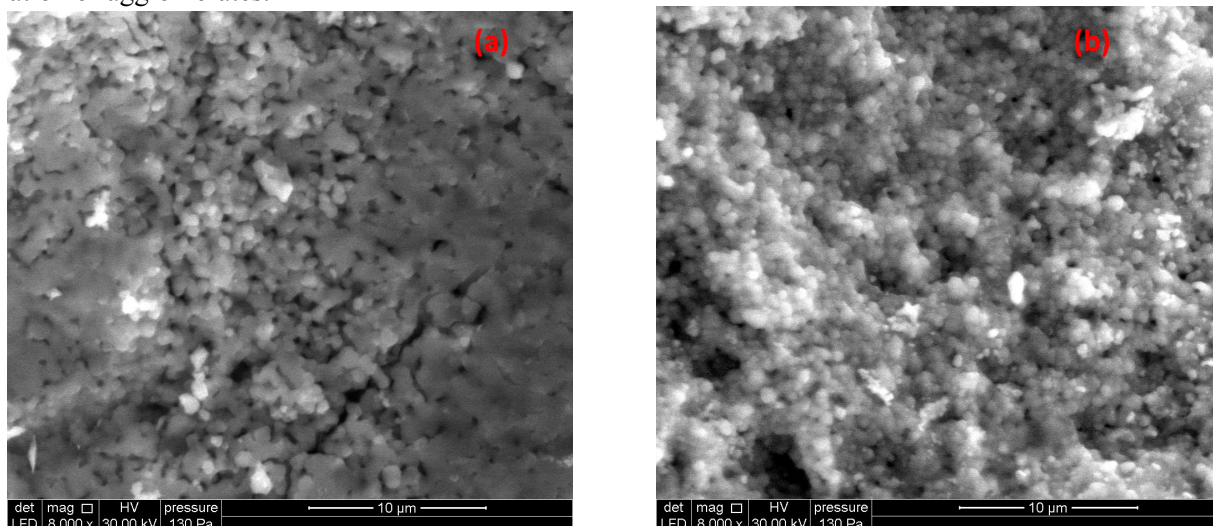


**Figure.6:** Scanning Electron Micrographs (SEM) for BS<sub>20</sub>T (a) and BS<sub>30</sub>T (b)

### 3.3. Dielectric studies

#### 3.3.1. Curie temperature and phase transitions

$\text{BaTiO}_3$  is known as a typical ferroelectric material with three phase transitions: tetragonal-cubic at about  $125^\circ\text{C}$ , orthorhombic-tetragonal around  $5^\circ\text{C}$  and orthorhombic-rhombohedral at approximately  $-90^\circ\text{C}$  [22]. In order to investigate the dielectric properties of the BST samples, the latter were prepared under the form of discs with a diameter of about  $10\ \text{mm}$  and a thickness of about  $1.2\ \text{mm}$ , followed by a sintering process at  $1200^\circ\text{C}$  for 6 hours.

The dielectric properties were studied as functions of temperature and for different frequencies ( $20\ \text{Hz}$ - $1\ \text{MHz}$ ). Figures 7 and 8 show the thermal behavior, for different frequencies, of the real part of the permittivity,  $\epsilon'_r$ , and dielectric losses for  $\text{Ba}_{1-x}\text{Sr}_x\text{TiO}_3$  ( $x = 0.00; 0.10; 0.20; 0.30$  and  $0.40$ ). Sharp peaks (maximum of  $\epsilon'_r(T)$ ) are observed for  $x = 0$  and  $0.10$  at the temperatures  $T_c = 125.3^\circ\text{C}$  and  $95.7^\circ\text{C}$ , respectively, corresponding to the ferro-to-paraelectric phase transition (Fig. 7a). This maximum becomes more diffuse ( $x > 0.10$ ) and shifts to lower values of temperature with increasing  $x$  (Figs. 7a and 7b). At the ferro-to-paraelectric transition (driven by temperature), the BST materials undergo a symmetry change from tetragonal to cubic, and this 'high-temperature' phase is almost always more disordered, i.e., has a higher symmetry than the 'low-temperature' phase. Our studied compositions of Sr doped  $\text{BaTiO}_3$  (disorder is introduced by Sr ions) show tetragonal (undoped sample) or pseudo-cubic structures, as confirmed by XRD and Raman studies, and the observed ferro-to-paraelectric phase transitions are consistent with the structural studies.

We also observe that  $(\epsilon'_r)_{\text{max}}$  (maximum of the permittivity at the transition temperature) decreases with increasing frequency in the considered interval, from  $20$  to  $50\ \text{kHz}$  (Fig. 7a) and from  $100$  to  $1000\ \text{kHz}$  (Figs. 7), and that for  $x > 0.10$  this decrease is accompanied with relaxation (Figs. 7) [23]. Moreover, an anomaly is observed above the transition temperature in the permittivity curves of the samples with  $x = 0.00, 0.10, 0.20$  (Fig. 7a), which may be due to an extrinsic phenomenon [24].

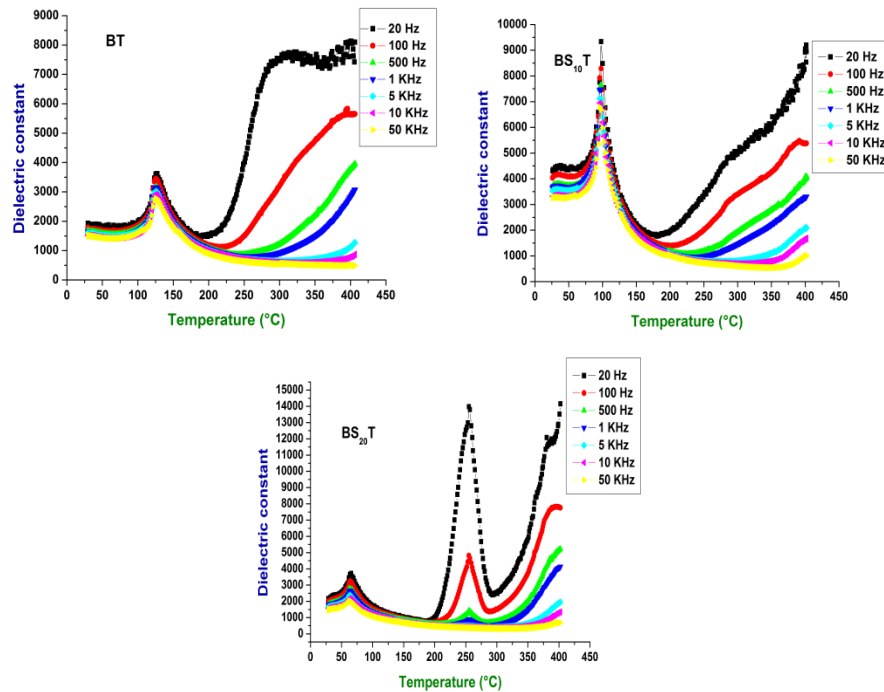


**Figure 7.a :** Variation of the real part of permittivity ( $\epsilon_r$ ) with temperature at different frequencies (20 Hz-50 KHz) for the  $\text{Ba}_{1-x}\text{Sr}_x\text{TiO}_3$  sintered at 1200 °C for 6 h.

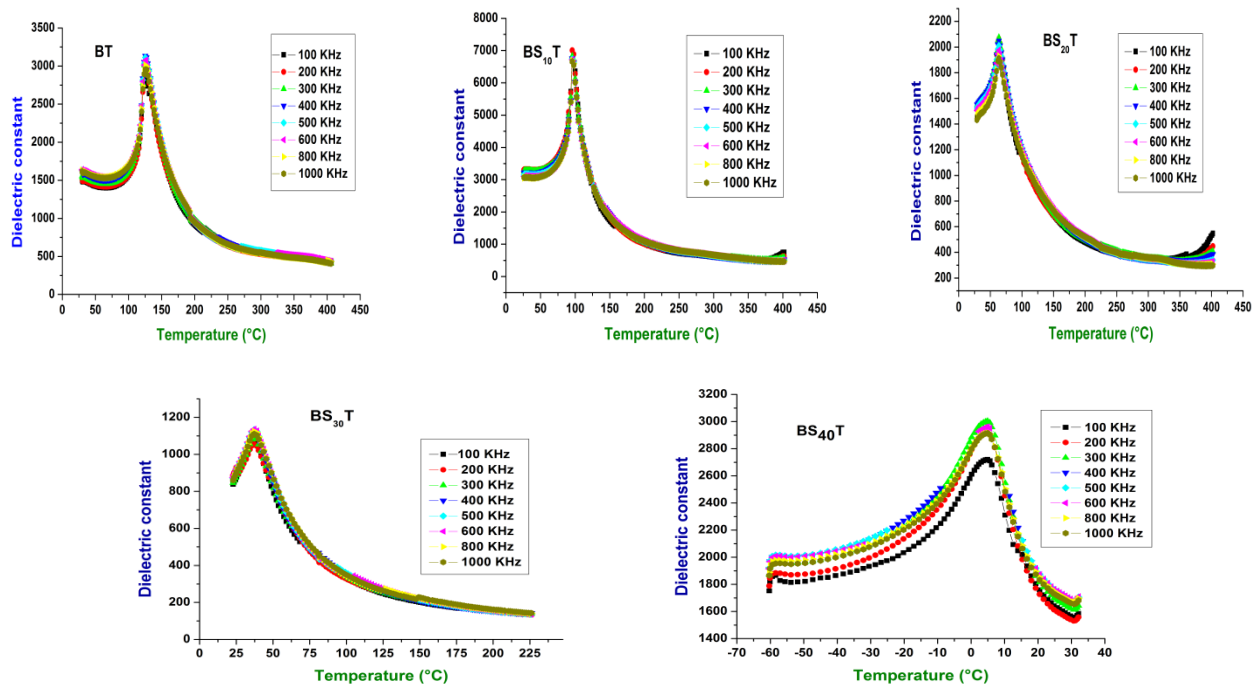


**Figure 7.b :** Variation of the real part of permittivity ( $\epsilon_r$ ) with temperature at different frequencies (100 kHz-1000 kHz) for the  $\text{Ba}_{1-x}\text{Sr}_x\text{TiO}_3$  sintered at 1200 °C for 6 h.

Thermal behavior of dielectric losses ( $\tan \delta$ ) is given in Figs. 8a and 8b. Low values of this parameter were recorded, with the appearance of a maximum around  $T_c$ . The strong increase of  $\tan \delta$  above  $T_c$  is consistent with the conductive character of the samples in the paraelectric phase. Table 3 gathers values of the dielectric parameters  $T_c$ ,  $\epsilon_r$  max and  $\tan \delta$  for  $\text{Ba}_{1-x}\text{Sr}_x\text{TiO}_3$  ceramics, together with some of those of the literature.

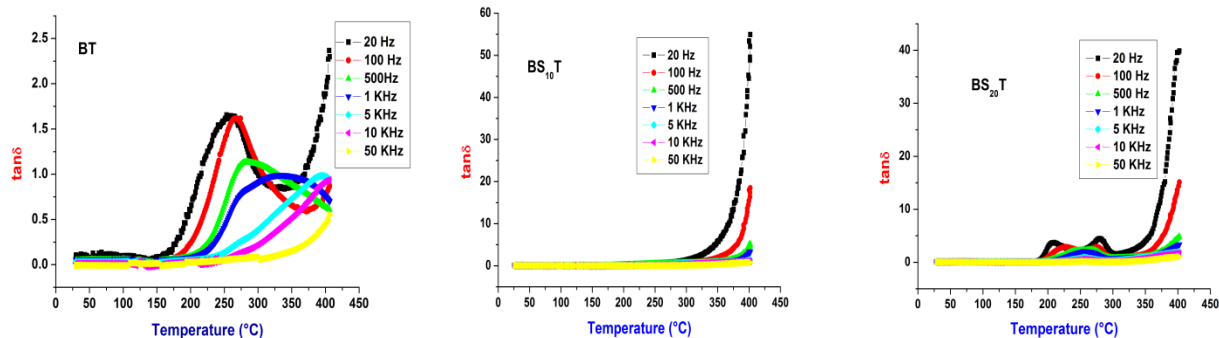


**Figure 8.a:** Variation of dielectric loss ( $\tan \delta$ ) with temperature at different frequencies (20 Hz-50 KHz) for  $\text{Ba}_{1-x}\text{Sr}_x\text{TiO}_3$  sintered at 1200 °C for 6 h.

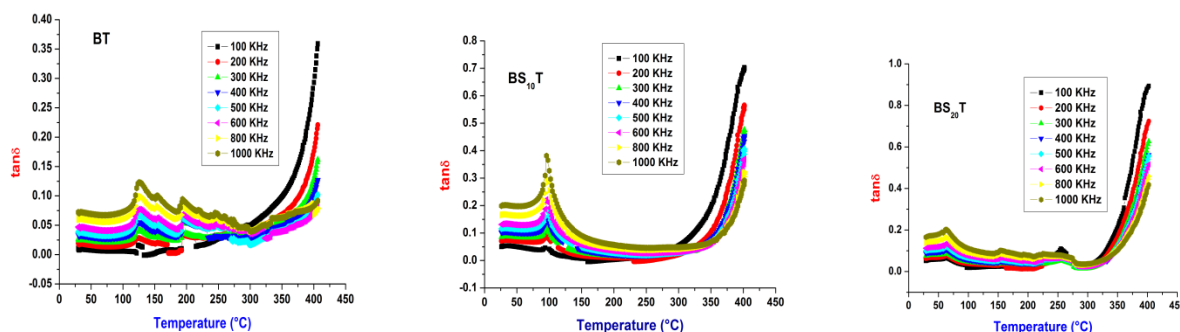


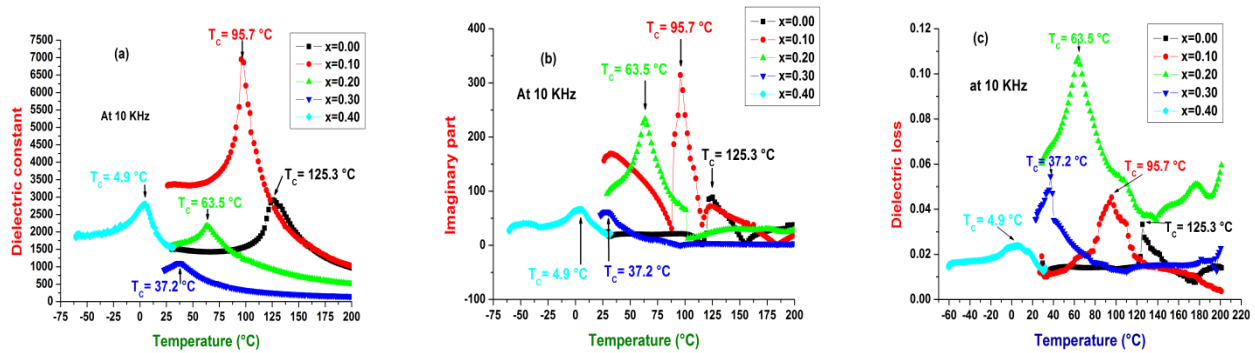
**Figure 8.b :** Variation of dielectric losses ( $\tan \delta$ ) with temperature at different frequencies (100 KHz-1000 KHz) for  $\text{Ba}_{1-x}\text{Sr}_x\text{TiO}_3$  sintered at 1200 °C for 6 h.

**Table 3:** Some  $\text{Ba}_{1-x}\text{Sr}_x\text{TiO}_3$  dielectric parameters compared with other studies.

Method of preparation	Ceramics	$T_f$ (Sintering)(°C)	$T_c$ (°C)	$\epsilon_r$	$\tan \delta$	Reference
Modified Pechini Sol-gel Sol-gel	$\text{BaTiO}_3$	1350 (3h)	125	7000(105 kHz)	0.025	Adelina.I et al[25]
		1300	112	3250(100kHz)	0.034	W.Li et al[29]
		1200(6h)	125.3	2915(10 kHz)	0.029	Present work
Sol-gel Sol-gel Sol-gel Sol-gel	$\text{Ba}_{0.9}\text{Sr}_{0.1}\text{TiO}_3$	1350(6h)	102	10800(100kHz)	0.038	Manoj.K et al[26]
		1400(4h)	109	5694(1kHz)	0.043	A.Lanculescu et al[28]
		1300	93	4160(100kHz)	0.032	W.Li et al[29]
		1200(6h)	95.7	6947(10 kHz)	0.045	Present work
Modified Pechini Sol-gel Sol-gel Sol-gel	$\text{Ba}_{0.8}\text{Sr}_{0.2}\text{TiO}_3$	1350 (3h)	64	5100(105kHz)	0.06	Adelina.I et al[25]
		1400(4h)	78	5638(1kHz)	0.039	A.Lanculescu et al[28]
		1300	64	4000(100kHz)	0.026	W.Li et al[29]
		1200(6h)	63.5	2182(10 kHz)	0.106	Present work
sol-gel Modified Pechini Sol-gel Sol-gel Sol-gel	$\text{Ba}_{0.7}\text{Sr}_{0.3}\text{TiO}_3$	1250	-(amb)	1564(1 kHz)	0.58	Chanyaphak.T et al [27]
		1350 (3h)	25	4000	0.0075	Adelina.I et al[25]
		1400(4h)	41	5482(1kHz)	0.038	A.Lanculescu et al[28]
		1300(2h)	40	3000(100kHz)	0.0275	W.Li et al[29]
		1200(6h)	37.2	1055(10 kHz)	0.057	Present work
Voie solide Sol-gel	$\text{Ba}_{0.6}\text{Sr}_{0.4}\text{TiO}_3$	1210(3h)	5	1500(1kHz)	0.026	L. Nedelcu et al [30]
		1200(6h)	4.9	2792(10 kHz)	0.0236	Present work

Figure 9 illustrates thermal variations of the dielectric parameters  $\epsilon'_r$ ,  $\epsilon''$  and  $\text{tg}\delta$ , of the sample  $\text{BS}_{0.20}\text{T}$ , at the frequency 10 kHz. These variations are consistent with literature [31]. Moreover, as the transition temperature

decreases with increasing x values, it is possible to obtain a ferroelectric material at a temperature near ambient temperature for a specific Sr concentration (in our case  $0.3 < x < 0.4$ ).



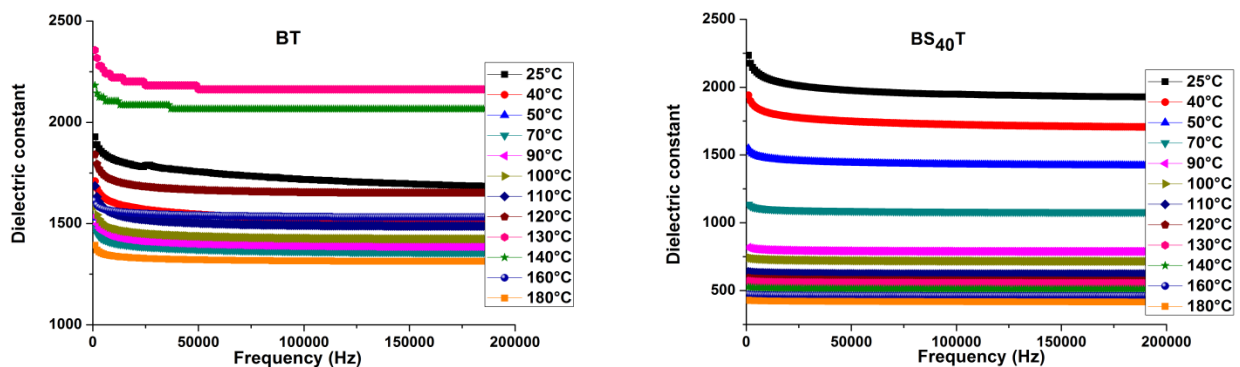
**Figure 9 :** Thermal variations of the real part  $\epsilon'_r$  (a), the imaginary part  $\epsilon''$  (b) of the permittivity and the dielectric loss (c) of the  $Ba_{1-x}Sr_xTiO_3$  at 10 kHz.

Figure 10 displays, as illustration, the frequency dependence of the permittivity,  $\epsilon_r$ , at different temperatures for BT and  $BS_{40}T$  samples; in the temperature range considered,  $\epsilon_r$  shows a gradual decrease with rise in frequency. This decrease is due to the space charges, leading to the high permittivity and frequency dispersion, and indicating a thermally activated nature of the observed dielectric relaxation.

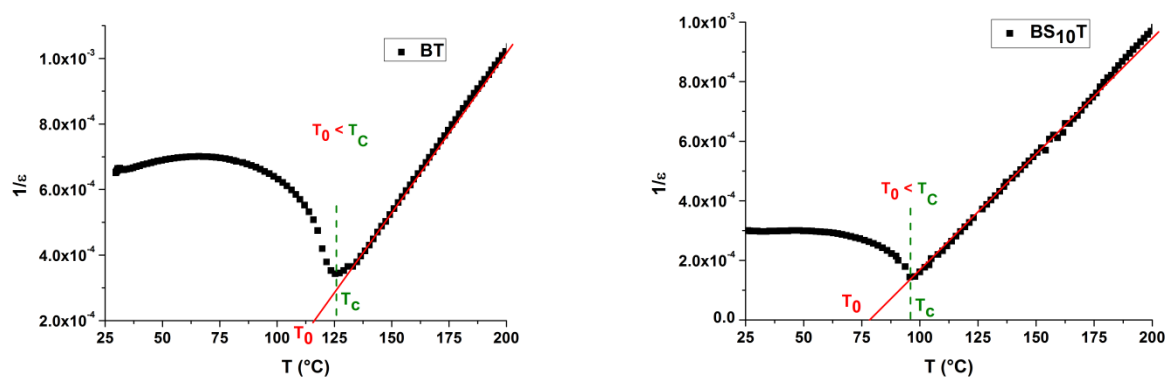
### 3.3.2. The ferroelectric-paraelectric phase transition and the Curie-Weiss law

Figure 11 depicts the thermal variation of the inverse of the permittivity ( $1/\epsilon_r$ ). It is known that for a normal ferroelectric the ferro-to-paraelectric phase transition is of first order when  $T_0 < T_C$  and a second order when  $T_C = T_0$ , where  $T_0$  is the Curie-Weiss temperature defined by the following relation [32]:

$$\frac{1}{\epsilon_r} = \frac{T - T_C}{C} \quad (2)$$



**Figure 10:** Frequency dependence of permittivity of BT and  $BS_{40}T$



**Figure 11:** Variation of  $1/\epsilon$  with temperature of the ceramics BT and  $BS_{10}T$  at 10 kHz.

The phase transition, which is of the first order for  $Ba_{1-x}Sr_xTiO_3$  such that  $x = 0.00$  and  $x = 0.10$ , transforms into the second order for the composition  $x = 0.40$  (Figure 11) [33].

Curie Weiss law is no longer valid in the case where relaxation and diffuseness are present. Modified Uchino's law is the appropriate approach to fit the permittivity behavior above the temperature of the ferro-to-paraelectric phase transition. [34] expressed as follows :

$$\frac{1}{\epsilon_r} = \frac{1}{\epsilon_{r \max}} \left[ 1 + \frac{(T - T_m)^\gamma}{2 * \delta^\gamma} \right] \quad (3)$$

Eq. 3 may be written under the following linear form:

$$\ln \left[ \left( \frac{\epsilon_{r \max}}{\epsilon_r} - 1 \right) * 2 \right] = \gamma \ln(T - T_m) - \gamma \ln \delta \quad (4)$$

Where :

$\gamma$  is an empirical coefficient that describes the diffuse nature of the transition.

$\gamma = 1$  for a conventional transition.

$1 < \gamma < 2$  for a diffuse transition.

$\gamma = 2$  for a relaxing ferroelectric, or totally diffuse.

$\delta$  indicates the degree of diffuseness of the peak

Figure 12 illustrates the fit of the data to Eq. 4. Figure 12 shows a linear relationship between  $\ln(T-T_m)$  and  $\ln(1/\epsilon_r - 1/\epsilon_{r \max})$  for the  $BS_xT$  samples at 10 kHz, with  $x = 0.40$ .

The increase of the  $\gamma$  factor (Table 4) shows that the phase transition becomes more diffuse with the increase of Sr content.

This diffuse phase transition can be influenced by factors such as disorder through local deformation and the fluctuation of microscopic composition [35]. The local strain may appear due to the ionic radius size of the site A ( $Ba^{2+}$  et  $Sr^{2+}$ ) and the ions of site B ( $Ti^{4+}$ ) of the perovskite structure  $ABO_3$ , which causes distortion of the  $TiO_6$  octahedron giving rise to electric fields and local deformations. Therefore, the value of  $\gamma$  depends on the crystal structure, and thus the defects in the ceramic.

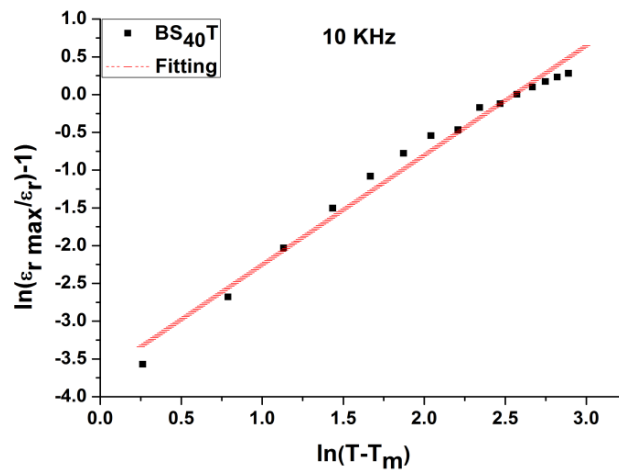


**Figure12:** Variation of  $\ln(1/\epsilon_r - 1/\epsilon_{r \max})$  as a function of  $\ln(T - T_m)$  for  $BS_{40}T$  ceramic.

**Table 4:** gathers  $\gamma$  values for  $BST_x$  samples.

Frequency (kHz)	$BS_{30}T$	$BS_{40}T$
1	1.1616	1.4895
10	1.1662	1.5550
50	1.1702	1.5092
100	1.1721	1.4177
200	1.1761	1.4583
400	1.1741	1.4576
600	1.1756	1.4512
800	1.1814	1.4403

1000	1.1834	1.4609
------	--------	--------

### 3.4. Complex impedance studies

In the perovskite system the main mode of charge transport is a multiple jump process. This jumping process occurs especially through the potential barriers that occur within the structure and the local atoms / ions environment.

In order to better understand the nature of conduction, we studied the complex impedance spectra of  $BS_xT$  samples. Figs. 13(a) and (b) show the impedance spectra ( $Z'' = f(Z')$ ) of  $BS_{10}T$  and  $BS_{20}T$  samples, sintered at 1200 °C for 6h, measured at different temperatures, from 335 to 400°C. For each temperature, the corresponding curves appear under the form of two depressed semicircles, suggesting the presence of both bulk and grain boundary effects in the studied samples. The high-frequency arc is related to the grain and the low-frequency arc to the grain boundary contribution. Impedance data from room temperature up to about 300 °C are not illustrated in Fig. 13 as they just showed a straight line with large slopes underlying the insulating character of the samples. It is observed on Fig. 13 that the slope of the lines decreases with increasing temperature, and hence they bend towards  $Z'$  axis, and that the corresponding radius of curvature decreases with increasing temperature, due to the increase of the conductivity of the samples.

The experimental data were adjusted using the Zview analysis software (version 3.1C), and the results are shown in Fig. 14, which are in good agreement with the experimental ones (Fig. 13). Moreover, each semicircle may be represented by an RC circuit, corresponding to individual component of the samples and providing a real representation of their electrical properties.

Results from impedance spectra have been approached by an equivalent circuit composed of two parallel elements (R, Q) connected in series, as shown in Fig. 15. R and Q represent the resistance and the constant phase element (CPE), respectively. Indeed, the fitting results show that the measured  $BS_xT$  capacitance response throughout the frequency range is not ideal, i.e., the  $BS_xT$  do not behave as pure capacitors, which may be due to the distribution of various relaxation times [36].

Hence, the effect of the grains (bulk) and the grain boundaries are represented by the parallel combinations R1-CPE1 and R2-CPE2, respectively.

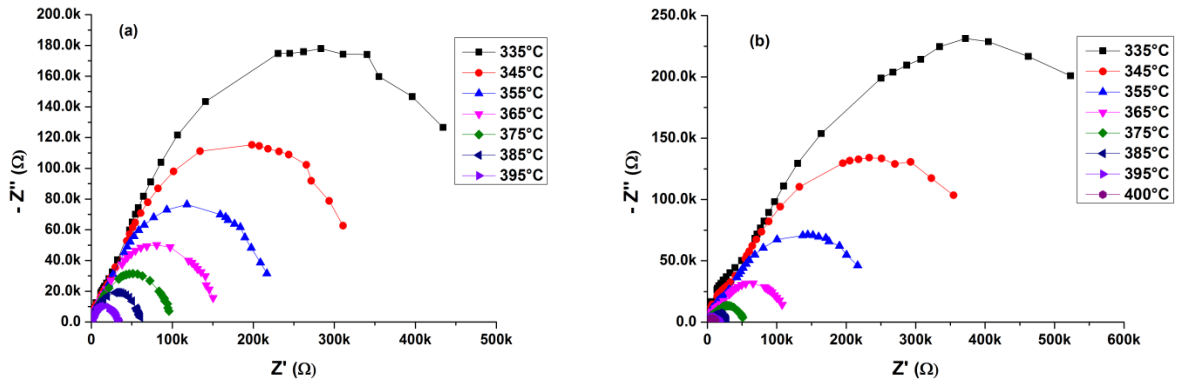


Figure 13: Impedance curves corresponding to  $BS_{10}T$  (a) and  $BS_{20}T$  (b).

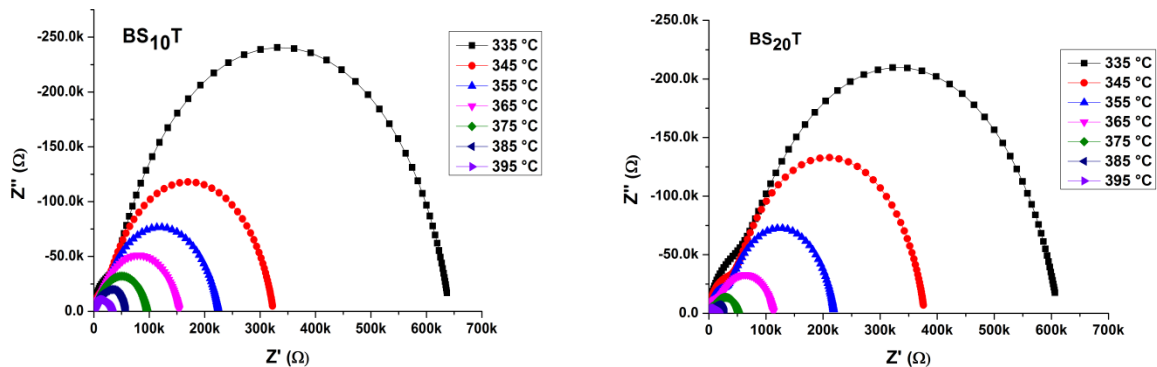


Figure 14:  $Z''$  as a function of  $Z'$  for the ceramics  $Ba_{1-x}Sr_xTiO_3$ .

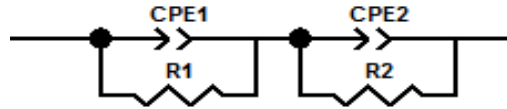


Figure 15: Equivalent circuit of the Ba<sub>1-x</sub>Sr<sub>x</sub>TiO<sub>3</sub> ceramic.

Values of these parameters have been obtained from impedance data (Table 5). The equivalent capacitance, C, of a constant phase element and the relaxation frequency  $f_{relax}$  corresponding to a specific (R,Q) element can be calculated according to the following equations [37]:

$$C = (R^{1-n}Q)^{\frac{1}{n}} \quad (4)$$

$$f_{relax} = \frac{(RQ)^{-1/n}}{2\pi} \quad (5)$$

R: resistance ( $\Omega$ )

Q: capacitance (F)

The value of the depression angle  $\theta$  (in radians) is calculated from the following equation [38]:

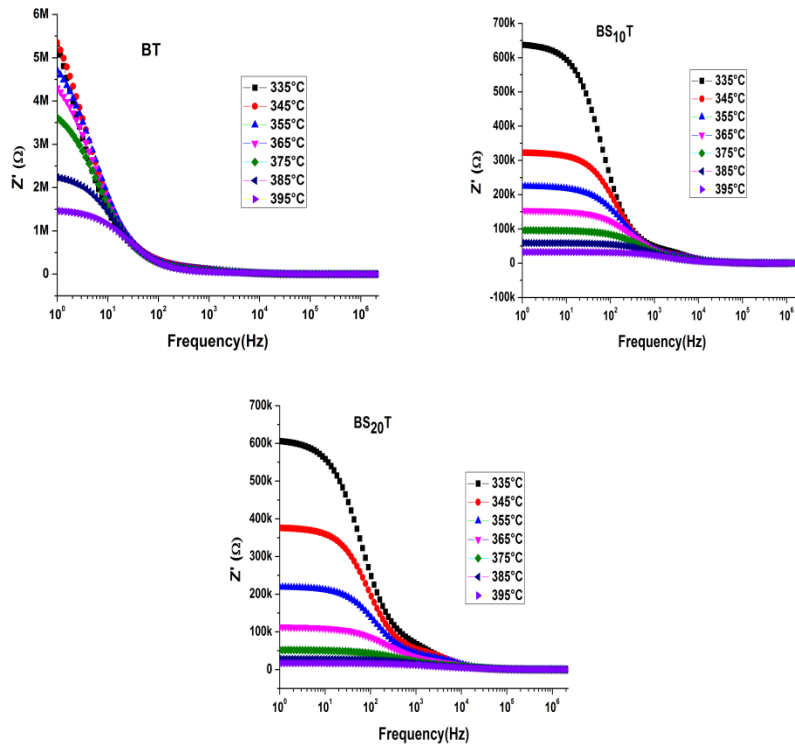
$$n = 1 - \frac{2\theta}{\pi} \quad (6)$$

Where n is the arc depression factor. The values  $n = 1$  and  $n = 0$  represent an ideal capacitor and an ideal resistance, respectively.

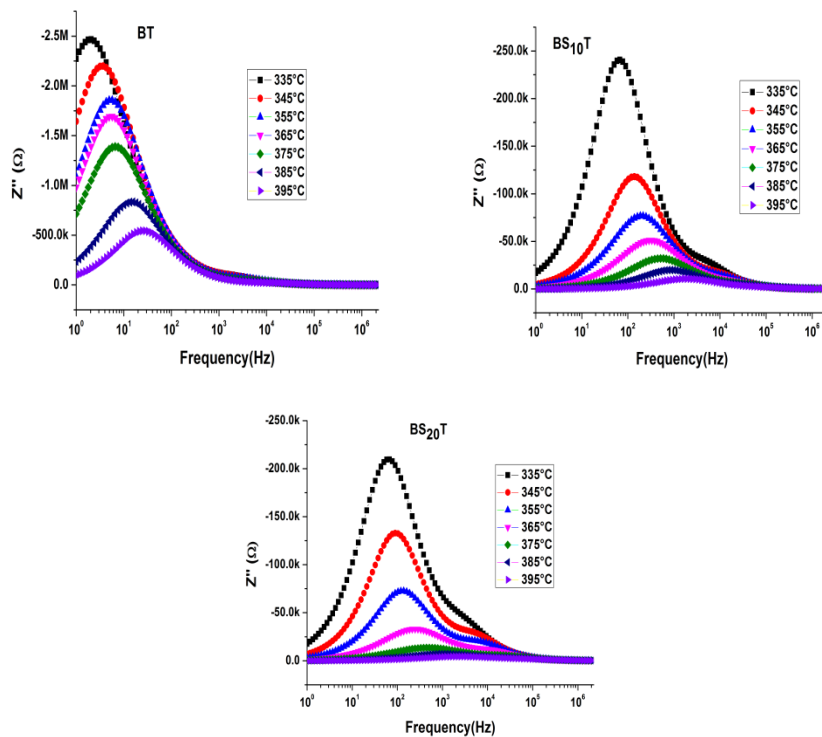
Table 5 gathers the obtained fitting parameters. The frequency dependence of  $Z'$  at different temperatures is shown in Figure 16-a. It is observed that  $Z'$  decreases with increasing frequency and temperature, indicating the increase in ac conduction ( $\sigma_{ac}$ ) in the samples. This increase in conduction may be explained as due to the contribution of defects such as oxygen deficiencies, and hence at high temperature, the contribution due to the latter is more dominant. At low frequencies, a significant decrease of  $Z'$  with increasing Sr content is observed. At high frequency, the value of  $Z'$  appears to be frequency independent for all temperatures, indicating that there is an increase in the concentration of defects with the rise of temperature leading to an increase of conductivity of the samples [39,40]. The merging of the  $Z'$  curves in the higher frequency region is probably due to the release of space charges due to the reduction of the barrier properties of the samples. It is also observed that the frequency for which the curves,  $Z'$ , coincide increases with the increase of the strontium content: 300 Hz for the pure BT and 40 kHz and 94 kHz for BS<sub>10</sub>T and BS<sub>20</sub>T, respectively.

Table 5: Estimated values of equivalent circuit parameters.

BS <sub>10</sub> T												
T (°C)	Q <sub>1</sub> (pF)	R <sub>1</sub> (k $\Omega$ )	n <sub>1</sub>	C <sub>1</sub> (nF)	$\tau_1$ (10 <sup>-6</sup> s)	f <sub>1max</sub> (Hz)	Q <sub>2</sub> (nF)	R <sub>2</sub> (k $\Omega$ )	n <sub>2</sub>	C <sub>2</sub> (nF)	$\tau_2$ (10 <sup>-4</sup> s)	f <sub>2max</sub> (Hz)
3 35	885	30.7	0.99	0.7958	27.2	6514.17	9.880	611	0.85	4.0099	60.4	65
345	923	18.8	0.99	0.8263	17.4	10245.85	11.500	305	0.84	3.9181	35.1	133.2
355	1012	13.3	0.99	0.9036	13.5	13243.1	16.400	212	0.80	3.9823	34.8	188.51
365	1073	7	0.99	0.9524	7.5	23871.68	19.600	147	0.77	3.4153	28.8	317
375	1075	5.1	0.99	0.9512	5.5	22808.25	19.900	91	0.78	3.3530	18.1	521.6
385	1078	4.8	0.97	0.7398	5.2	44817.64	18.517	54	0.81	3.6632	9.99	804.58
395	1395	1.5	0.98	1.0682	2.09	99325.2	24.027	31	0.77	2.7949	7.45	1836.8
BS <sub>20</sub> T												
T (°C)	Q <sub>1</sub> (pF)	R <sub>1</sub> (k $\Omega$ )	n <sub>1</sub>	C <sub>1</sub> (nF)	$\tau_1$ (10 <sup>-6</sup> s)	f <sub>1max</sub> (Hz)	Q <sub>2</sub> (nF)	R <sub>2</sub> (k $\Omega$ )	n <sub>2</sub>	C <sub>2</sub> (nF)	$\tau_2$ (10 <sup>-3</sup> s)	f <sub>2max</sub> (Hz)
3 35	2267	56	0.90	0.8366	127	3397.11	13.445	556	0.82	4.5898	7.47	62.37
345	1289	42.7	0.93	0.6161	55.1	6049.69	13.550	335	0.85	5.2296	4.54	90.85
355	1533	31.5	0.92	0.6459	48.3	7821.40	20.360	188	0.83	6.5120	3.83	130
365	1537	15.5	0.94	0.7791	23.8	13179.51	42.999	98	0.75	6.9452	4.21	233.83
375	1391	7	0.95	0.7578	9.74	30002.82	95.871	45.2	0.68	7.4064	4.33	475.82
385	2807	3.9	0.91	0.9070	10.9	44991.56	112.77	24.3	0.67	6.1314	2.74	1061.7
395	2782	1.98	0.93	1.1182	5.51	71884.43	129.41	15.2	0.65	4.5164	1.97	2318.4



**Figure 16.a:** variation of  $Z'$  as a function of the frequency for ceramics  $Ba_{1-x}Sr_xTiO_3$ .



**Figure 16.b:** Variation of  $Z''$  as a function of frequency for  $Ba_{1-x}Sr_xTiO_3$  ceramics.

The variation of the imaginary part of the impedance ( $Z''$ ) with the frequency at different temperatures is shown in Figure 16-b. It is observed that  $Z''$  increases with frequency, passes through a maximum that shifts towards higher frequencies on increasing both temperature and Sr content, and then decreases and tends to an almost constant value.

The width of the maximum may suggest the existence of a distribution of relaxation times [41] that can be calculated from the values of the angular frequencies corresponding to these maxima with the help of the following relation:

$$\tau = 1/\omega_{\max} \quad (8)$$

Figure 17 shows the variation of the relaxation time as a function of  $1000/T$ . Values of the obtained activation energies are gathered in Table 6.

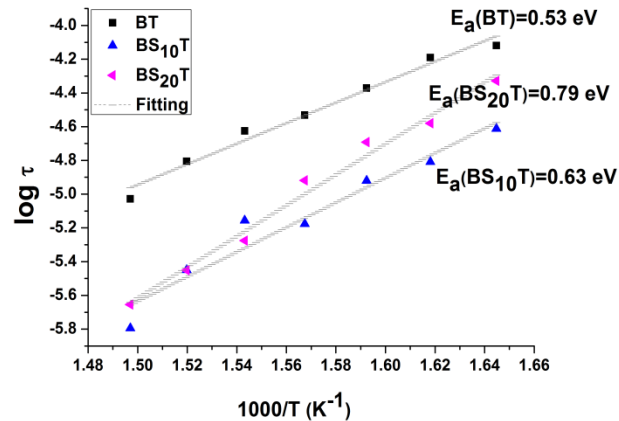


Figure 17: Variation of the relaxation time as a function of  $1000/T$

Table 6: Activation energy values obtained from Fig. 18

	BT	BS <sub>10</sub> T	BS <sub>20</sub> T
E <sub>a</sub> (eV)	0.53	0.63	0.79

### 3.5. Conductivity studies.

In order to better understand the transport mechanism in the BST ceramics, the thermal electrical conductivity behavior was investigated. The conduction in a material may be due to the migration of charge carriers over a long distance or to the relaxation bias mechanism over a short distance. In dielectric materials, which is our case, the electrical conductivity is mainly attributed to the jump of polarons in the material.

The electrical conductivity can be determined from the dielectric data with the help of the following relation:

$$\sigma = 2\pi f \epsilon_0 \epsilon'' \quad (9)$$

Where  $f$  is the frequency (Hz),  $\epsilon_0$  is the permittivity of vacuum ( $8.854 \times 10^{-12}$  F/m) and  $\epsilon''$  is the imaginary part of the dielectric permittivity.

Fig. 18 shows, as illustration, the frequency dependence of the conductivity, at different temperatures, for BT and BS<sub>20</sub>T.

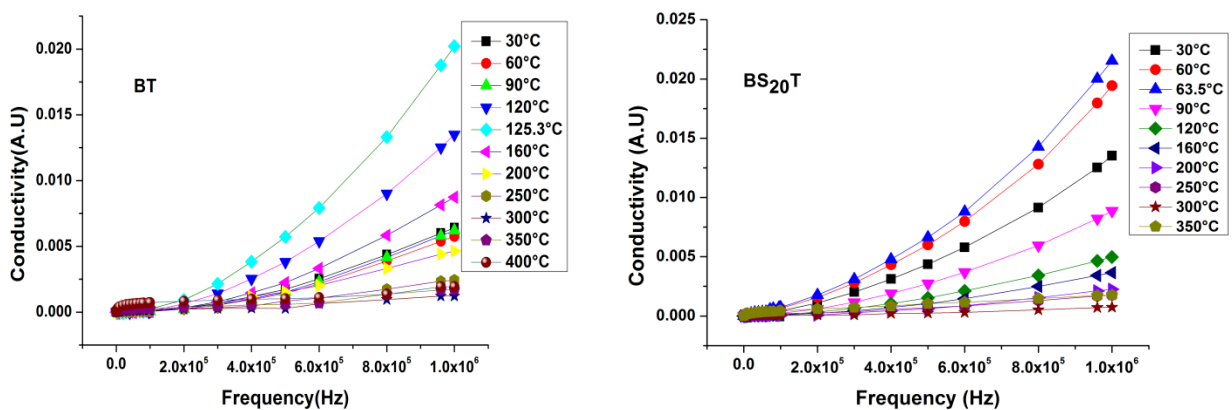


Figure 18: Variation of conductivity as a function of frequency for  $Ba_{1-x}Sr_xTiO_3$  ceramics, with  $x = 0$  and  $0.20$

It is noted that with increasing frequency,  $\sigma$  shows an almost frequency independent behavior followed by a dispersion above a certain frequency (region where  $\sigma$  is sensitive to both frequency and temperature) [42]; the observed increase may be attributed to the relaxation phenomenon. Moreover, for a given frequency,  $\sigma$  increases first with temperature until the ferro-to-paraelectric transition temperature and then decreases.

Figure 19 displays the variation of  $\sigma$  as a function of  $1000/T$ , for  $BS_{20}T$  below and above the transition temperature.

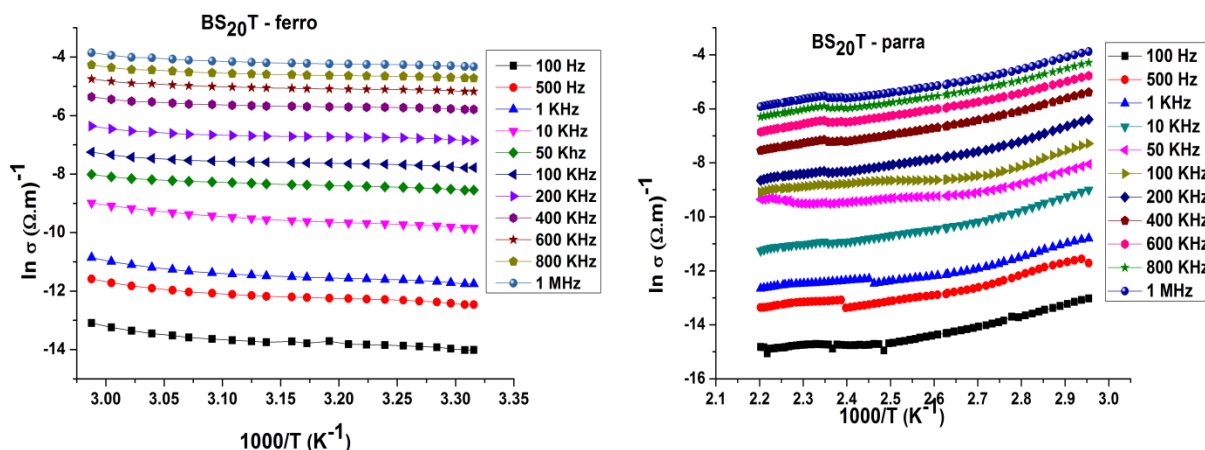


Fig. 19: Variation of the conductivity as a function of  $1000/T$

It is observed that  $\sigma$  first increases (below  $T_c$ ) with increasing temperature, and then, above  $T_c$ , decreases. This behavior, in accordance with that observed on Fig. 18, may be explained as due to the existence of the Positive Temperature Coefficient of Resistivity (PTCR effect).

Indeed, as revealed by the curves corresponding to thermal variations of resistivity (Fig. 20(a and b)), the latter decreases until  $T_c$  and then increases. This effect is maximum for the sample with 20% in Sr. A good PTCR material should have a high ratio of the maximum electrical resistivity to the minimum room temperature resistivity and high capability to maintain its high electrical resistivity over the long range of temperature above its Curie point. In doped  $BaTiO_3$  ceramics the PTCR jumps by 3 to 7 orders of magnitude. This jump for the  $BS_{10}T$  sample is about 3.5 order of magnitude, and may be improved through optimizations and processing and its different related parameters.

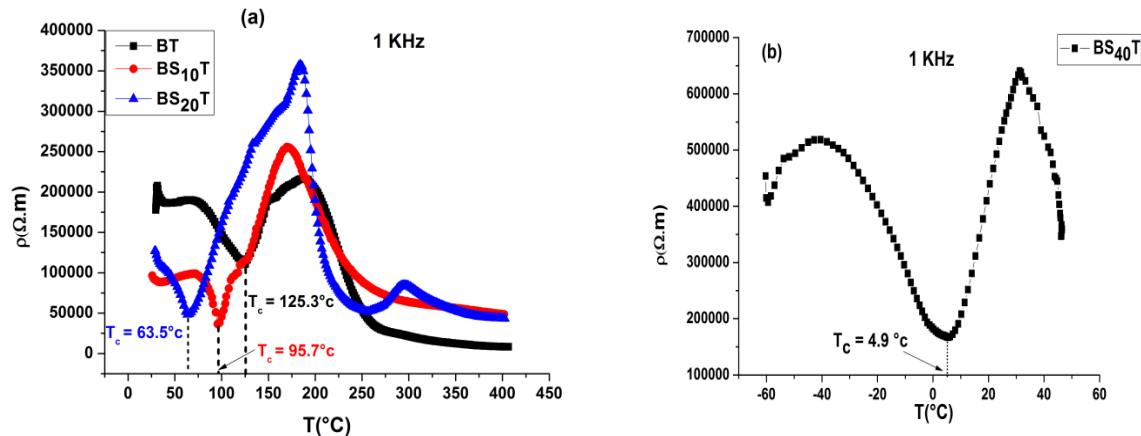


Figure. 20: Thermal variation of resistivity of samples: (a) BT,  $BS_{10}T$ ,  $BS_{20}T$  and (b)  $BS_{40}T$

### 3.6. Modulus spectra

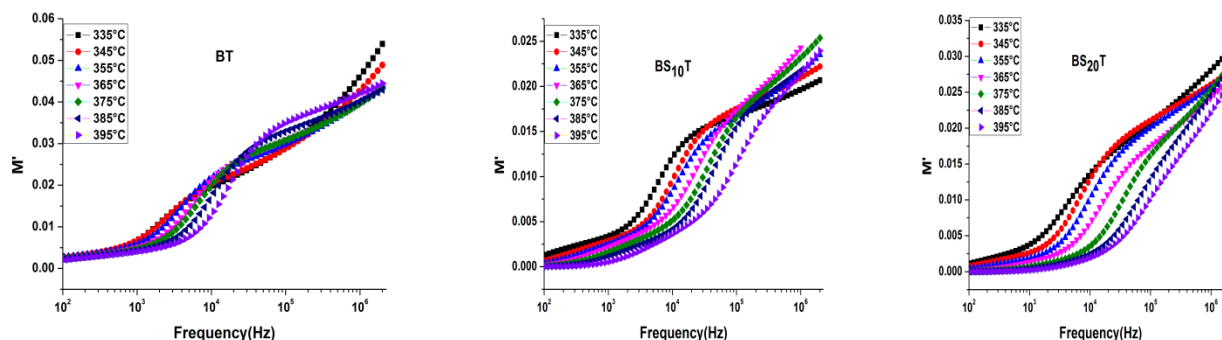
Analysis and interpretation of the dynamic aspects of electric transport phenomena may be carried out with the help of complex modulus which provides informations about the electrical processes characterized by the smallest capacity of the material, the representation of the electric modulus suppresses the undesirable effects of extrinsic relaxation. Indeed, in the  $M^*$  formalism, the spatial charge effects and polarization of the electrodes and the grain-boundary conduction process can be suppressed [43, 44].

The complex electrical modulus ( $M^*$ ) is defined as a function of complex dielectric permittivity ( $\epsilon^*$ ) by the following relation:

$$M^* = \frac{\epsilon'}{\epsilon'^2 + \epsilon''^2} + i \frac{\epsilon''}{\epsilon'^2 + \epsilon''^2} = M' + iM'' \quad (7)$$

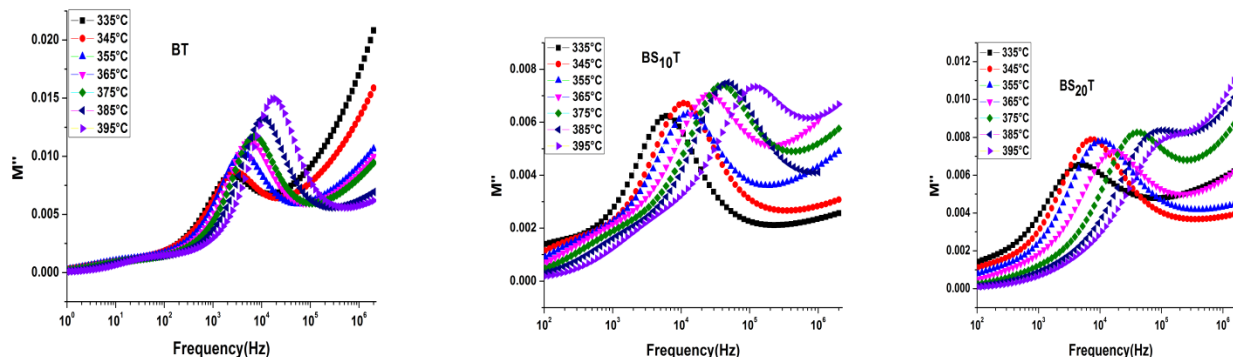
Or  $M'$  and  $M''$  are respectively the real and imaginary part of the complex electric modulus  $M^*$

Figure 21 shows the variation of the real part of the electric modulus ( $M'$ ) as a function of frequency, at high temperatures (between 335 °C and 395 °C). Low values of  $M'$  are observed in the low frequency region followed by a continuous dispersion with increasing frequency. It is also observed that the obtained curves may be approached by three plateaus (Fig. 21), the first and the third having approximately the same slope. After a first slight increase (first plateau), a quite strong change in the slope is observed (second plateau) within a certain frequency interval, followed by a second change in slope leading to a similar tendency (similar slope) of increase as of the first plateau; a 'break' in the behavior occurs in a certain domain of frequency probably due to the short range mobility of carriers such as ions. Moreover,  $M'$  shows a dispersion tending towards  $M'_{(infini)}$ , the asymptotic value of  $M'$  at high frequencies.



**Figure 21:** Variation of  $M'$  as a function of frequency for  $Ba_{1-x}Sr_xTiO_3$  ceramics.

Figure 22 shows the frequency dependence of the imaginary part,  $M''$ , of the electric modulus at different temperatures.  $M''$  exhibits a maximum which shifts to higher frequencies with increase in temperature. This peak observed in the plot of  $M''$  as a function of frequency corresponds to a relaxation process. The frequency region below this maximum of  $M''$  gives the extent to which charge carriers are mobile on long distances (Jump conduction process). At the frequencies above this maximum the carriers are confined to potential wells and hence are mobile on short distances [45].



**Figure 22 :** Variation of  $M''$  as a function of frequency for  $Ba_{1-x}Sr_xTiO_3$  ceramics.

Moreover, the widening of the observed asymmetric peak (Fig. 22) may be related to the existence of a distribution of relaxation times. The frequency  $\omega_{max}$  (corresponding to  $M''_{max}$ ) gives the relaxation time  $\tau$  from the condition  $\omega_{max} \cdot \tau = 1$ . Taking into account this condition, Figure 23 displays variation of relaxation time as a function of  $1000/T$ . As for this parameter calculated from  $Z''$  data, the activation energy increases with increasing Sr content, and its corresponding values are quite similar to those obtained from fitting of  $M''$  data to an Arrhenius law (Fig. 23).

### 3.7. Study of the piezoelectric properties of BSxT.

Piezoelectric study has been carried out on the sample  $BS_{10}T$ .

The piezoelectric coefficients were determined using the resonance-antiresonance frequencies from figure 24, for each temperature [46, 47].

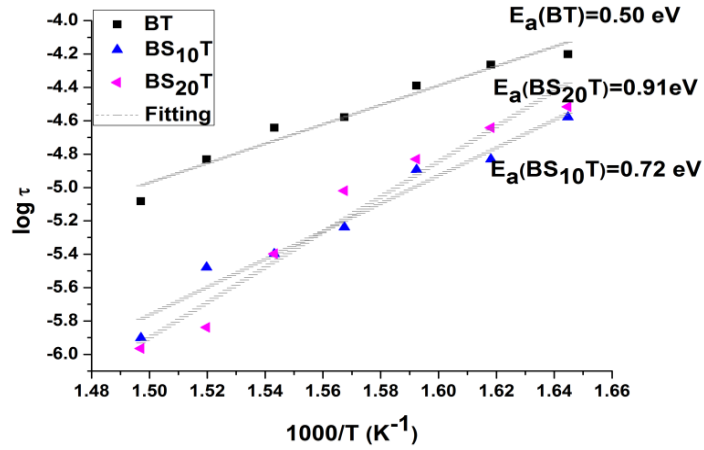


Figure 23: Variations of relaxation time as functions of 1000/T for BT, BS<sub>10</sub>T and BS<sub>20</sub>T

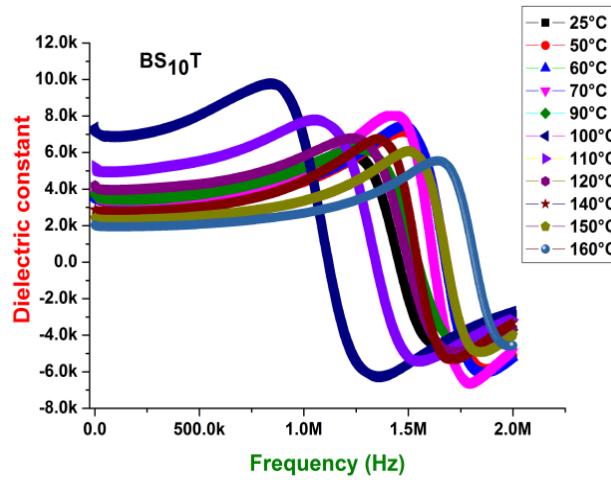


Figure 24 : Variation of dielectric permittivity with frequency for BS<sub>10</sub>T sintered at 1200 °C

The planar electromechanical coupling factor  $K_p$  was determined with the help of the following relation:

$$K_p^2 = \frac{\eta^2 - (1 - \alpha^{E^2})}{2(1 + \alpha^E)} * \frac{f_a^2 - f_r^2}{f_a^2} = 1.255 * \frac{f_a^2 - f_r^2}{f_a^2} \quad (10)$$

Young Module E

$$E = \left[ \frac{\pi \phi f_r}{\eta} \right]^2 * (1 - \alpha^{E^2}) * d(N/m^2) \quad (11)$$

The piezoelectric constant of charge d

$$d^A = K_p^A \sqrt{\frac{(1 - \alpha^E) \epsilon_r \epsilon_0}{2E}} (C/N) \text{ à } 25^\circ C \quad (12)$$

The voltage constant g

$$g^A = \frac{d^A}{\epsilon_r \epsilon_0} (m.V / N) \text{ à } 25^\circ C \quad (13)$$

Calculation of the piezoelectric charge constant  $d^B$  and the voltage constant  $g^B$  at high temperatures was done using the following relations:

$$d^B = d^A \frac{K_P^B f_r^A}{K_P^A f_r^B} * \sqrt{\frac{\epsilon_r^A}{\epsilon_r^B}} \quad (14) \quad \text{and} \quad g^B = \frac{d^B}{\epsilon_0 \epsilon_r^B} \quad (15)$$

With:

- $\Phi$ : Diameter of the sample (m)
- $\alpha^E$ : The poisson coefficient (0.31 for ceramics)
- $\eta$ : The root of the Bessel equation ( $\eta = 2.05$ )
- d: Density ( $\text{Kg} / \text{m}^3$ )
- $\epsilon_0$ : is the permittivity of free space ( $8.854 \times 10^{-12} \text{ F/m}$ )
- $\epsilon_r$ : The relative permittivity
- $f_r$ : Resonance Frequency(Hz)
- $f_a$ : Anti-resonance frequency(Hz)

**Table 7:** gathers values of the piezoelectric parameters of the sample BS<sub>10</sub>T heat treated at 1200°C.

BS <sub>10</sub> T (1200°C)	T (°C)	f <sub>r</sub> (MHz)	f <sub>a</sub> (MHz)	ε <sub>r</sub>	K <sub>p</sub>	E (10 <sup>12</sup> N.m <sup>-2</sup> )	d <sup>B</sup> (10 <sup>-12</sup> C.N <sup>-1</sup> )	g <sup>B</sup> (10 <sup>-3</sup> V.m.N <sup>-1</sup> )
	50	1.477	1.873	7101	0.69	2.78737	50.44659	0.80264
	60	1.485	1.865	7412	0.68	2.81764	48.31719	0.73657
	70	1.43	1.794	8092	0.68	2.61279	47.93066	0.66925
	90	1.271	1.774	6218	0.78	2.06407	71.07194	1.29142
	100	0.829	1.342	9763	0.88	0.87809	98.02649	1.13448
	110	1.073	1.563	7782	0.81	1.47107	78.43805	1.1389
	120	1.238	1.728	6779	0.78	1.95828	69.88494	1.16477
	140	1.355	1.706	6732	0.68	2.34591	55.80408	0.93668
	150	1.502	1.845	6063	0.65	2.88252	50.70086	0.94484
160	1.64	1.98	5550	0.63	3.43653	46.82705	0.95335	

The planar electromechanical coupling factor K<sub>p</sub>, represents the ability of a ceramic to transform electrical energy into mechanical energy. Values given in Table 7 show that this factor increases first with increasing temperature and reaches its maximum value around the ferro-to-paraelectric transition (96°C) and then decreases. The increase in K<sub>p</sub> may be due to the fact that during the polarization of the material the degree of alignment of the domains increases (K<sub>p</sub> increases) and becomes higher in the coexisting region of the cubic and tetragonal phases. The decrease of K<sub>p</sub> may be due to the fact that the increase in temperature favors the mobility of the ions, which causes a disorder of the dipole moments which are randomly oriented.

In the same time, the young's modulus shows a decrease with temperature until its minimum value in the vicinity of T<sub>c</sub>. Beyond this value there is an increase of this factor. The decrease of this factor as a function of temperature may be due to the rupture of some bonds in the material, and thus the attraction forces prevent the vibration of the dipoles [48].

The piezoelectric coefficient of charge, d<sup>B</sup>, follows the same variations as of K<sub>p</sub> (Table 7); this coefficient also reaches its maximum value around T<sub>c</sub> and then decreases. This decrease may be due to thermal agitations that are responsible for the disorder in the material.

It is clear from then that optimum values of dielectric permittivity and piezoelectric parameters are observed around the ferro-to-paraelectric transition temperature.

## Conclusion

Structural, dielectric and piezoelectric properties of sol gel processed Ba<sub>1-x</sub>Sr<sub>x</sub>TiO<sub>3</sub> (x = 0.00; 0.10; 0.20; 0.30 and 0.40) nanopowders were investigated. Pure perovskite structure was obtained under heating at 900°C during 3h. Sr doping transforms the structure of the pure sample (BaTiO<sub>3</sub>) from quadratic to pseudocubic. The average crystallite size was about 30 nm. Dielectric studies reveal that Sr doping lowers the temperature of the ferro-to-paraelectric transition accompanied with relaxation and diffuseness for x > 0.10. Modified Uchino's law was used to describe the thermal paraelectric behavior of the permittivity. Investigation of the conduction phenomenon in these samples reveals the presence of the PTCR effect, which was prominent for x = 0.20. Optimum values of the piezoelectric parameters were obtained around the Curie temperature.

## References

1. L.H. Parker, A.F. Tasch, IEEE Circuits Devices Mag. 6 (1990) 17-26.
2. T. Kawaguchi, H. Adachi, K. Setsune, O.Y. Amazaki, K. Wasa, Appl. Opt. 23 (1984) 2187-2191.
3. K.K. Deb, Ferroelectrics 82 (1998) 45-53.
4. L.A. Thomas, Ferroelectrics 3 (1972) 231-238.

5. D.Y. Lu, Y. Yue, X.Y. Sun, *J. Alloys Compd.* 586 (2014) 136-141.
6. S.K. Rout, J. Bera, in: A.P. Tandon (Ed.), Allied Publishers Pvt. Ltd., New Delhi. (2004) 3-7.
7. C. Fu, C. Yang, H. Chen, Y. Wang, L. Hu, *Mater. Sci. Eng. B.*, 119 (2005) 185-188.
8. O.P. Thakur, C. Prakash, D.K. Agarwal, *Mater. Sci. Eng., B.* 96 (2002) 221-225.
9. R.M. Mahani, I.K. Battisha, M. Alyb, A.B. AbouHamad, *J. Alloys Compd.* 508 (2010) 354-358.
10. M. Veith, S.MTHUR, N. LECERF, V. Huch, T. Decker. *J. Sol-Gel Sci. technol.* 15 (2000) 145-158.
11. L. Wei, X. Zhijun, C. Ruiqing, F. Peng, H. Jigong, *J. Alloys Compd.* 482 (2009) 137-140.
12. D. Fengtao, C. Bin, C. Hualei, N. Ruiyuan, C. Zhuguo, *Mater. Res. Bull.* 44 (2009) 1930-1934.
13. P. M.M. Vijatović, J.D. Bobić, T. Ramoška, J. Banys, B.D. Stojanović, *Mater. charact.* 62 ( 2011 ) 1000-1006.
14. A. Elbasset, F. Abdi, T. Lamcharfi, S. Sayouri, M. Aillerie. *IREPHY.* No.3, 7 (2013) 287-293.
15. B.D. Cullity, *Elements of X-ray diffraction*, Addison-Wesley publishing Company Inc., 1956.
16. E. V. Ramana, F. Figueiras, A. Mahajan, D. M. Tobaldi, B.F.O. Costa, M.P.F. Graça and M. A. Valente. *J. Mater. Chem. C*, 4(2016) 1066-1079.
17. J.T. Last, *Phys. Rev.*, 105 (1957) 1740-50.
18. N.W. Alock, V.M. Tracy, and T.C. Waddington, *J. Chem. Soc., Dalton Trans.*, (1976) 2243-46.
19. E. Sanchez, T. Lopez, R. Gomea, A. Morales and O. Novaro, *J. Solid State Chem.*, 122 (1996) 309-14.
20. U.D. Venkateswaran, V.M. Naik, R. Naik, *Phys. Rev. B.* 58 (1998) 14256-60.
21. P. Hermet, M. Veithen, P. Ghosez, *J. Phys.: Condens. Matter.* 21 (2009) 215901.
22. Y. Xu, *Ferroelectric Materials and Their Applications*. North-Holland: Amsterdam, 1991.
23. A. Helmi, H. Khemakhem, G. V'elu, J.C. Carru, R.V.D. M'uhll, *Solid State Sci.* 6 (2004) 1347-1351.
24. B. S. Kang, S. K. Shoi and C. H. Park, *J. Appl. Phys.* 94 (3)(2003)1904-1911.
25. I. Adelina, B. Daniela, V. Massimo, E.C. Cristina, M. Liliana, V. Eugeniu, D. Nicolae, C. Dorel, *J. Eur. Ceram. Soc.* 27 (2007) 3655-3658.
26. K. Manoj, G. Ashish, K. Ravi, M.C. Bhatnagar, *Physica B* 403 (2008)1819-1823.
27. T. Chanyaphak, T. Sarawut, *Ceram. Int.* 41(2015) S95-S99.
28. A. Ianculescu, I. Pintilie, C.A. Vasilescu, M. Botea, A. Iuga, A. Melinescu, N. Dragan, L. Pintilie, *Ceram. Int.* 42 (2016) 10338-10348.
29. L. Wei, X. Zhijun, C. Ruiqing, F. Peng, H. Jigong, *J. Alloys Compd.* 499 (2010) 255-258
30. L. Nedelcu, A. Ioachim, M. Toacsan, M.G. Banciu, I. Pasuk, C. Berbecaru, H.V. Alexandru, *Thin Solid Films* 519 (2011) 5811-5815.
31. S. Lahiry, A. Mansingh, *Thin Solid Films* 516 (2008) 1656-1662.
32. M.E. Lines, A.M. Glass, *Principles and Applications of Ferroelectrics and Related Materials*, Oxford University Press, Oxford, 1977.
33. J. Ravez, A. Simon, *CR Acad. Sci.* 325 (1997) 481.
34. N.S. Echadou, T. Lamcharfi, S. Sayouri, L. Hajji, A. Alimoussa, *Phys. Chem. News*, 26 (2005) 40-46.
35. L.E. Cross, *Ferroelectrics* 151 (1994) 305.
36. A.R. Muhammad, N.R. Muhammad, K.V. Sarvanan, *Ceram. Int.* 41 (2015) 11436-11444.
37. D. Chen, R.Ran, K. Zhang, J. Wang, Z. Shao, *J. Power Sources* 188 (2009) 96.
38. K. Prabakar, S.A.K. Narayandass, D. Mangalaraj, *Cryst. Res. Technol.* 37 (2002) 1094.
39. A.A. Saif, P. Poopalan, *Physica B*, 406 (2011) 1283-1288.
40. S. Sen, R.N.P. Choudhary, *Mater.Chem.Phys.* 87(2-3) (2004) 256-263.
41. A.K. Jonscher, The universal dielectric response, *Nature* 267(5613) (1977) 673-679.
42. S.R. Elliot, *Philos. Mag.* 36 (1977) 1291.
43. R.M. Neagu, E. Neagu, *J. Appl. Phys.* 88 (11) (2000) 6669.
44. S.A. Saafan, S.A. Seoud, R.E. El Shafer, *Physica B* 365 (2005) 27.
45. C.R.K. Mohan, R. Dey, S. P. Patel, R.K. Pandey, M.P. Sharma, P.K. Bajpai, *Nucl. Instrum. Methods Phys. Res. B.* 372 (2016) 50-57.
46. B.JAFFE, S. ROTH R, S. MARZULLO, *J. Res. Natl. Bur. Stand.* 55 (1955) 239- 254.
47. W. P. MASON, H. JAFFE, *Proceedings of the IRE.*, No.6, 42 (1954) 921-930.
48. A. Boutarfaia, S.E. Bouaoud, *Ceram. Int.*, No.4, 22 (1996) 281-286.

(2017) ; <http://www.jmaterenvironsci.com>